

# Bulk Contact Between Silver Nanowires Top Electrode and Interface Layer Enables High Performance of Full-Solution-Processed Semitransparent Organic Solar Cell Module

Wusong Zha, Li-Min Chen, Shaoming Sun, Xiaomei Gao, Yunfei Han, Tong Liu, Qun Luo,\* Yu-Chiang Chao, Hsiao-Wen Zan, Hsin-Fei Meng,\* Xiaozhang Zhu, and Chang-Qi Ma\*

The solution-processed electrode is key to the full-solution-processed organic solar cells (OSCs). Silver nanowires (AgNWs) are considered as an attractive solution-processed electrode due to their low sheet resistance and high transmittance. However, the traditional “line-plane” contact between AgNWs and the interface buffer layer is insufficient, resulting in the low performance of full-solution-processed OSCs. Herein, a bulk contact structure is reported between AgNWs and interface, formed by inserting the interface layer material, such as  $\text{HMoO}_x$  (hydrogen molybdenum bronze) into the AgNWs networks. The extra  $\text{HMoO}_x$  can be connected with the bottom interface buffer layer, forming a longitudinal network, and wrapping the AgNWs in the longitudinal interfacial layer. This bulk contact electrode-interface structure increases the area of AgNWs/interface layers, promoting charge transfer and collection. Besides, the top-injected method can enable the formation of a water-based ink film on the top of the organic layer, as well as avoid solvent erosion between AgNWs and the interface layer. Based on the bulk contact electrode-interface structure, this work realized high performance of 12.27% and 9.54% for  $0.09 \text{ cm}^2$  small-area device and  $10.8 \text{ cm}^2$  full-solution-processed semitransparent mini-module. These results provide a new idea for full-solution-processed OSCs preparation.

semiconductor materials and interface engineering,<sup>[5,6]</sup> the power conversion efficiency (PCE) of single-junction OSCs has exceeded 19%.<sup>[7,8]</sup> Besides, compared with traditional inorganic or hybrid perovskite photovoltaics, the organic photovoltaic materials can be designed to have a wavelength-selective absorption.<sup>[9]</sup> Thus, with organic semiconductors, the semitransparent OPVs with different colors can be fabricated, showing a good application prospect in the building-integrated photovoltaics (BIPVs) and modern agriculture greenhouses.<sup>[10–12]</sup>

For the full-solution-processed OSCs, the solution-processed top electrode is the key.<sup>[13]</sup> Several kinds of solution-processed electrodes toward full-solution-processed OSCs, including organic high conductivity polymer PEDOT:PSS,<sup>[14–16]</sup> carbon nanotubes,<sup>[17]</sup> graphene,<sup>[18]</sup> and silver nanowires (AgNWs)<sup>[19–21]</sup> have been developed. Among them, the AgNWs are considered as the most attractive candidate due to their low sheet resistance ( $R_{sq}$ ) and


high transmittance. Generally, the sheet resistance of the AgNWs electrode is  $10\text{--}20 \Omega \square^{-1}$ ,<sup>[22]</sup> and the transmittance of the corresponding electrode is around 85–92%.<sup>[23]</sup> In addition, the AgNWs electrode has good compatibility with a variety of printing processes, such as spray coating,<sup>[24]</sup> inkjet printing,<sup>[25]</sup> and gravure printing.<sup>[26]</sup> Compared with the evaporated thin-silver

## 1. Introduction

Organic solar cells (OSCs) have attracted wide attention in the field of new-generation photovoltaic cells because of their flexibility,<sup>[1]</sup> lightweight,<sup>[2]</sup> rich color,<sup>[3]</sup> and suitability for roll-to-roll process.<sup>[4]</sup> With the continuous development of organic

W. Zha, Q. Luo, C.-Q. Ma  
School of Nano-Tech and Nano-Bionics  
University of Science and Technology of China  
Hefei 230027, P. R. China  
E-mail: qluo2011@sinano.ac.cn; cqma2011@sinano.ac.cn

W. Zha, X. Gao, Y. Han, Q. Luo, C.-Q. Ma  
i-Lab & Printable Electronics Research Center  
Suzhou Institute of Nano-Tech and Nano-Bionics  
Chinese Academy of Sciences (CAS)  
Suzhou 215123, P. R. China

 The ORCID identification number(s) for the author(s) of this article can be found under <https://doi.org/10.1002/solr.202300322>.

DOI: 10.1002/solr.202300322

L.-M. Chen  
Department of Electro-Physics  
National Yang Ming Chiao Tung University  
Hsinchu 300, Taiwan

S. Sun, X. Zhu  
Beijing National Laboratory for Molecular Sciences  
CAS Key Laboratory of Organic Solids Institute of Chemistry  
Chinese Academy of Sciences,  
Beijing 100190, P. R. China

T. Liu  
Vacuum Interconnected Nanotech Workstation (Nano-X)  
Suzhou Institute of Nano-Tech and Nano-Bionics  
Chinese Academy of Sciences (CAS)  
Suzhou 215123, P. R. China

or sputtered indium tin oxide (ITO) transparent electrode, the solution-processed AgNWs avoid the use of the high vacuum equipment, which can effectively reduce the cost of transparent electrodes for semitransparent OSCs.

The silver nanowires are usually stacked randomly, with gaps remaining in the AgNWs electrode.<sup>[26,27]</sup> Though the disordered stacking of AgNWs leads to high transmittance of the AgNWs electrode, it causes high sheet resistance of the electrode as well.<sup>[28,29]</sup> To get a compact stacking nanowire network, several solutions have been developed. The first strategy is removing polyvinylpyrrolidone (PVP) from the silver nanowires' surface. During the synthesis of silver nanowires, PVP plays two crucial roles as a structure-directing agent and stabilizer.<sup>[30]</sup> However, the existence of nonconductive PVP causes large contact resistance between silver nanowires. So, the removal of PVP from the surface of AgNWs through NaBH<sub>4</sub> treatment<sup>[31]</sup> or high-temperature annealing<sup>[32]</sup> is developed. The second method is welding the silver nanowire through various approaches. For the poor contacts among the adjacent silver nanowires junction, the welding method can decrease the electrode sheet resistance and enhance mechanical stability. For instance, Park et al. utilized the plasmonic to weld silver nanowires,<sup>[33]</sup> realizing a low sheet resistance ( $\approx 5 \Omega \square^{-1}$ ) and high transparency (90%) AgNWs electrode. Besides, based on chemical welding, Zeng et al. adopted a reductive ionic liquid to reduce Ag<sup>+</sup>, realizing the atomic-level chemical welding of AgNWs.<sup>[34]</sup> Xiong et al. immersed the AgNWs film with silver–ammonia and glucose mixed solution,<sup>[35]</sup> and the chemical welding occurs on the silver nanowires network, reducing the contact resistance between silver nanowires. Building a composited electrode is also a good way to increase AgNWs electrode conductivity. For example, Huang et al. utilized the aluminum-doped zinc oxide (AZO) and AgNWs to build a ferroconcrete-like AZO@silver nanowire ((AgNWs)@AZO) composite electrode.<sup>[36]</sup> The  $R_{sq}$  of the obtained AgNWs@AZO electrode decreases significantly from 1863.1 to 16.2  $\Omega \square^{-1}$ . Analogously, Chen et al. utilized ITO nanoparticles to fill the silver nanowires network building a composite electrode.<sup>[37]</sup> The transparent metal oxide filler can not only decrease the electrode sheet resistance but also have a slight effect on its transmittance. Analogously, Jagadamma et al. demonstrated that the deposition of MoO<sub>3</sub> can also reduce the sheet resistance of the composited electrode.<sup>[38]</sup> Although all of the above methods can improve the conductivity of AgNWs electrodes, interface contact between the electrode and interface buffer layer is also a deciding factor of charge transport and collection,

which is rarely studied. Additionally, in full-solution-processed OSCs with AgNWs deposited on the top of the buff layer, the interface buffer layer suffers from solvent erosion,<sup>[39]</sup> further weakening the interfacial charge transport.

In this work, a bulk contact electrode-interface structure was proposed to improve interface charge transport and avoid solvent erosion between AgNWs and the interface layer in the full-solution-processed OSCs. Specifically, the bulk contact top electrode structure was composed of the printed AgNWs networks and penetrative interface materials, which were formed through permeating the interface layer into the preformed AgNWs networks. In comparison with the regular planar contact of the top AgNWs electrodes and the interface layer, the bulk contact top electrode greatly reduced the charge transport resistance and improve the device performance. Additionally, since the interface layer was deposited followed by the AgNWs, the predeposited AgNWs could effectively regulate the surface energy, and thereby the aqueous PEDOT:PSS (AI 4083) could be successfully deposited on the top of the organic active layer. Based on the structure of ITO/ZnO/PBDB-T-2F:L8-BO/HTLAgNWs-HMoO<sub>x</sub> (Hydrogen molybdenum bronze), the full-solution-processed semitransparent OSCs with the area of 0.09 cm<sup>2</sup> gave a high efficiency of 12.27% and the mini-module with the area of 10.8 cm<sup>2</sup> gave an efficiency of 9.54%.

## 2. Results and Discussion

### 2.1. Construction and Characterization of Bulk Contact Electrode-Interface Structure

In this work, we fabricated the inverted OSCs with ITO, ZnO, HMoO<sub>x</sub>:PEDOT:PSS, AgNWs as the bottom electrode, electron transporting layer (ETL), hole transporting layer (HTL), and the top electrodes. As a traditional structure, the AgNWs top electrode is deposited directly on the interface layer (electron or hole transport layer).<sup>[40]</sup> Since the AgNWs are one-dimensional materials with strand diameter and length of about 30 nm and 30  $\mu$ m, the disordered stacking of AgNWs on the surface of the buffer layer usually has a small contact area, which could be regarded as a “line-plane” contact as shown as **Figure 1a** (I). In this “line-plane” contact structure, the contact area between the AgNWs electrode and the interface buffer layer is much smaller than the planar contact of the interface layer and the vacuum-deposited metal electrode. In addition, the random stacking of AgNWs resulted in loose contact between the AgNWs electrode and the interface layer.<sup>[41–43]</sup> As a comparison, the bulk contact between the AgNWs and the interface layer was fabricated by injecting an additional interfacial layer into the gaps of the AgNWs electrode (as shown by **Figure 1a** (II)). Accordingly, a bulk contact electrode-interface structure was formed between the AgNWs electrode and the interface buffer layer, as shown in **Figure 1a** (III). In this bulk contact electrode structure, the predeposited interface materials and the later deposited interface materials would form a continuous connection from the surface to bottom, and the AgNWs electrode is wrapped by the interface buffer layer, which greatly increases the contact area between the AgNWs electrode and the interface layer.

Y.-C. Chao  
Department of Physics  
National Taiwan Normal University  
Taipei 106, Taiwan

H.-W. Zan  
Department of Photonics  
National Yang Ming Chiao Tung University  
Hsinchu 300, Taiwan

H.-F. Meng  
Institute of Physics  
National Yang Ming Chiao Tung University  
Hsinchu 300, Taiwan  
E-mail: meng@nycu.edu.tw

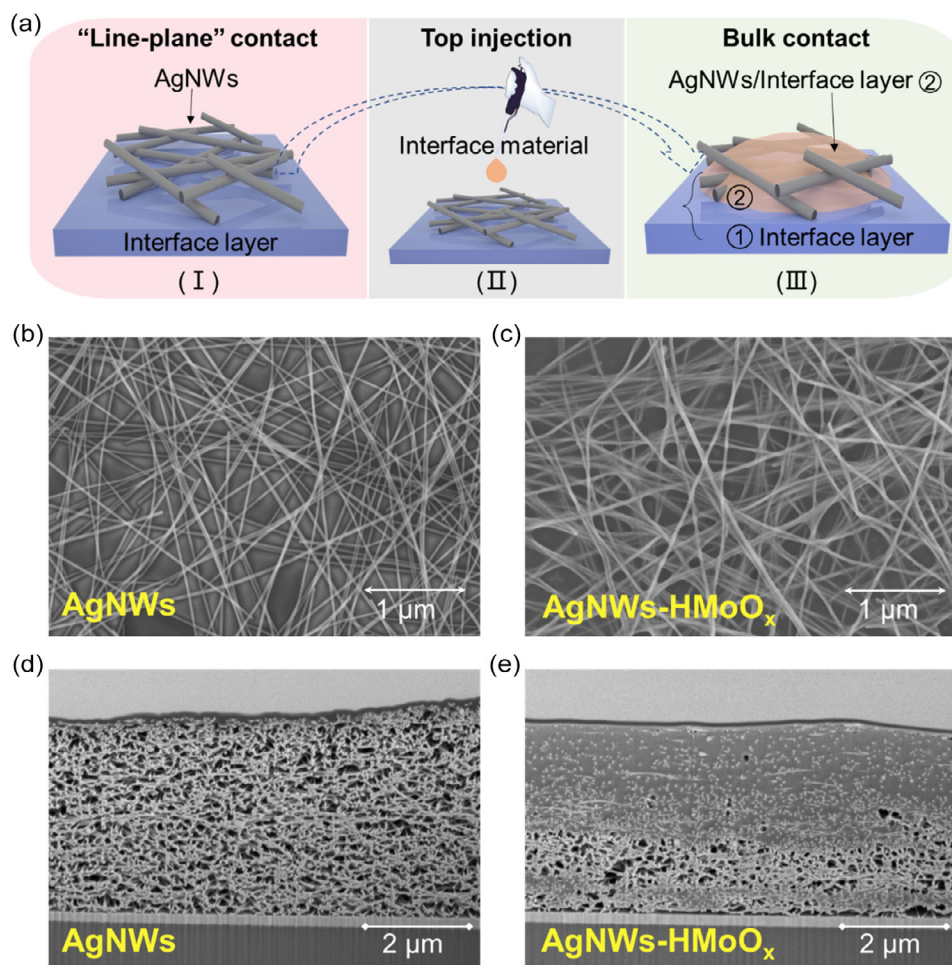


**Figure 1.** a) The schematic diagram of bulk contact between AgNWs and interface layer; b,c) surface and d,e) section images of SEM AgNWs and AgNWs:HMoO<sub>x</sub> structure.

The formation of the bulk contact electrode-interface structure was proved by scanning electron microscopy (SEM) images. The hydrogen molybdenum bronze (HMoO<sub>x</sub>) is selected due to its high work function, good conductivity, and solubility of alcohol, which can be deposited on the active layer with a low-temperature postprocessing. Figure 1b,c shows the surface morphology and the cross-section SEM images of the two different structures. As shown in Figure 1b, the AgNWs electrode randomly stack with relatively large voids among the AgNWs networks. After the deposition of HMoO<sub>x</sub> HTL material, the AgNWs were collected by the HMoO<sub>x</sub>, and arranged like a spider web (as shown in Figure 1c). To exclude the influence of solvent, the SEM image of the AgNWs electrode treated by ethanol was also shown in Figure S1a,b, Supporting Information. The SEM image showed the solvent treatment has negligible influence. This observation ruled out the impact of the solvent effect, demonstrating that the formation of a “spider web” connection in AgNWs:HMoO<sub>x</sub> was attributed to the HMoO<sub>x</sub> nanoparticles. This observation indicated the HMoO<sub>x</sub> interfacial material could partially fill the void in the AgNWs electrode and wrap the Ag nanowires. To show the filling effect of HMoO<sub>x</sub> clearly, thick

AgNWs samples about 3 μm were made, and Figure 1d,e shows the cross-sections SEM image of the electrode-interface structures. As shown by Figure 1d, there are obvious voids in the AgNWs electrode, which provide a path for the injection of interface materials. In contrast, Figure 1e indicates the voids of AgNWs are nearly filled by the HMoO<sub>x</sub> even though the thickness of HMoO<sub>x</sub> filling was increased to higher than 1 μm, which is much thicker than the thickness of AgNWs electrode (about 120 nm) in the device. This observation strongly indicated the HMoO<sub>x</sub> nanoparticles can permeate into the AgNWs networks.

**Figure 2a,b** exhibits the effect of HMoO<sub>x</sub> concentration on the conductivity and transmission of AgNWs electrodes. With HMoO<sub>x</sub> concentration increasing from 0 (only ethanol treatment) to 10 mg mL<sup>-1</sup>, the average sheet resistance ( $R_{sq}$ ) of AgNWs electrode slightly increased from 7.39 Ω □<sup>-1</sup> (0, ethanol) to 7.71 Ω □<sup>-1</sup> (2 mg mL<sup>-1</sup>), 8.06 Ω □<sup>-1</sup> (5 mg mL<sup>-1</sup>), and 8.76 Ω □<sup>-1</sup> (10 mg mL<sup>-1</sup>). Notably, the  $R_{sq}$  of ethanol treatment AgNWs is lower than that of the original AgNWs electrode, relating to the solvent effect of ethanol.<sup>[13]</sup> In addition, the light transmittance of the AgNWs electrodes is shown in Figure 2b. Though the transmittance of the AgNWs electrode could reach

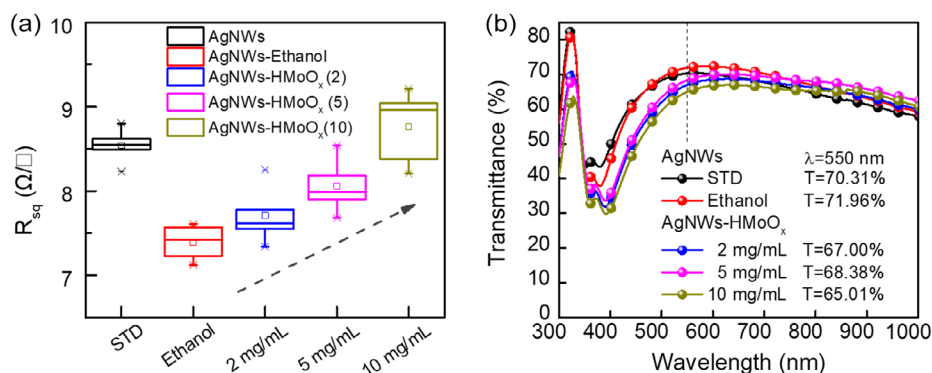


**Figure 2.** The a) sheet resistance and b) transmittance of the AgNWs-HMoO<sub>x</sub> electrodes with HMoO<sub>x</sub> with different concentrations.

as higher as 90%,<sup>[26]</sup> the optimized electrodes for the semitransparent OSCs showed a relatively low transmission of around 70%. Increasing the transmittance of the top AgNWs electrode would cause low optical usage and large sheet resistance of electrode, which lead to the decrease of  $J_{SC}$  and FF. After the HMoO<sub>x</sub> deposition, the transmission of the AgNWs electrode decreased from 71.96% (with ethanol treatment) to 67.00% (2 mg mL<sup>-1</sup>), 68.38% (5 mg mL<sup>-1</sup>), and 65.01% (10 mg mL<sup>-1</sup>). Based on these results, the conduction of AgNWs electrode was not improved for the bulk contact structure.

## 2.2. Full-Solution-Processed OSCs Based on Bulk Contact Electrode-Interface Structure

To investigate the device performance with different top electrode structures, four kinds of OSCs were fabricated, and the specific preparation methods are listed in the Supporting Information. As shown in **Figure 3a–d**, structure A is an inverted OSC with a structure of ITO/ZnO/active layer/HTL(HMoO<sub>x</sub>:PEDOT:PSS)/AgNWs. Structure B is an inverted OSC without HTL. Both the AgNWs electrodes with structures A and B are treated with ethanol. Structure C is a kind of device with AgNWs deposited first and followed by HMoO<sub>x</sub> deposition. Structure D is prepared by depositing HMoO<sub>x</sub> on the AgNWs electrode of structure A. The PBDB-T-2F:L8-BO blend films are selected as the active layer, of which the molecular structures are shown in **Figure 3e**. **Figure 3f** shows the  $J$ - $V$  curves of four kinds of devices (structure A–D). For the  $J$ - $V$  curves measurement of the devices, the light is illuminated from ITO side, and their specific parameters are listed in **Table 1**.

In structure A, the AgNWs electrode was deposited directly on the HTL. The device with such a “line-plane” contact of electrode-interface structure gave an optimized open-circuit voltage ( $V_{OC}$ ) of 0.869 V, a short circuit current density ( $J_{SC}$ ) of 18.49 mA cm<sup>-2</sup>, and a fill factor (FF) of 71.01%, resulting in a power conversion efficiency (PCE) of 11.41%. In contrast to structure A, structure B is a kind of device without HTL, where the electrode is deposited directly on the active layer. As a result,  $V_{OC}$ ,  $J_{SC}$ , and FF decrease sharply, and the device cannot nearly work, which indicates the necessity of HTL for full-solution-processed OSCs. Keep this in mind, it is interesting to find structure C showed a normal  $V_{OC}$  of

0.820 V. Since in structure C, the HMoO<sub>x</sub> was deposited after the AgNWs electrode, the normal  $V_{OC}$  of this device proved the HMoO<sub>x</sub> could permeate into the AgNWs networks and direct contact with the organic photoactive layer to form an effective organic/HTL interface. Nevertheless, for structure C, the contact resistance between HTL and the organic photoactive layer might be relatively high, thereby  $J_{SC}$ , FF, and PCE of the device are lower than the normal device. Whereas, this result strongly suggested that such a bulk contact structure that formed through predepositing AgNWs networks and followed by permeating the HTL into the AgNWs is possible to achieve the full-solution-processed OSCs. Based on the result of structure C, the OSCs with structure D were fabricated, which contained a compact HMoO<sub>x</sub>:PEDOT:PSS HTL and a bulk-contact AgNWs:HTL structure. The  $V_{OC}$  of structure D is 0.878 V, the  $J_{SC}$  is 18.64%, and the FF is 74.97%. The PCE of the device is 12.27%, which is higher than that of structure A (11.41%). Taking devices A and D for comparison, the FF was significantly improved from 71.01% to 74.97%. We have known the HMoO<sub>x</sub> treatment of the AgNWs gave a higher sheet resistance relative to the pristine AgNWs electrode. However, the series resistance ( $R_s$ ) of the devices decreased from 5.1 for structure A to 4.6 Ω cm<sup>2</sup> for structure D. These observations demonstrated improvement of device performance for the bulk contact electrode-interface structure originates from reduced interface contact resistance rather than the improvement of AgNWs conduction. Therefore, we could make a speculation that such a bulk contact was an effective structure to improve the interface charge transport between the AgNWs networks electrode and the interface layer. Besides, **Figure S2**, Supporting Information, shows the transmission of four different structures (A–D). The average transmittance of four structure devices has no significant difference (A: 20.51%, B: 20.96%, C: 20.86%, and D: 20.36%), and the specific value is also listed in **Table 1**. After that, **Figure S3**, Supporting Information, shows the evolution of the performance parameters of structure A and structure D under continuous illumination, and the device of structure D shows a lower decay rate. **Figure 3g** shows the EQE results of devices A, C, and D, and the result showed that the difference between the integral current value and the measured short-circuit current density is less than 5%. The EQE spectra of device B are absent because this device cannot work normally.



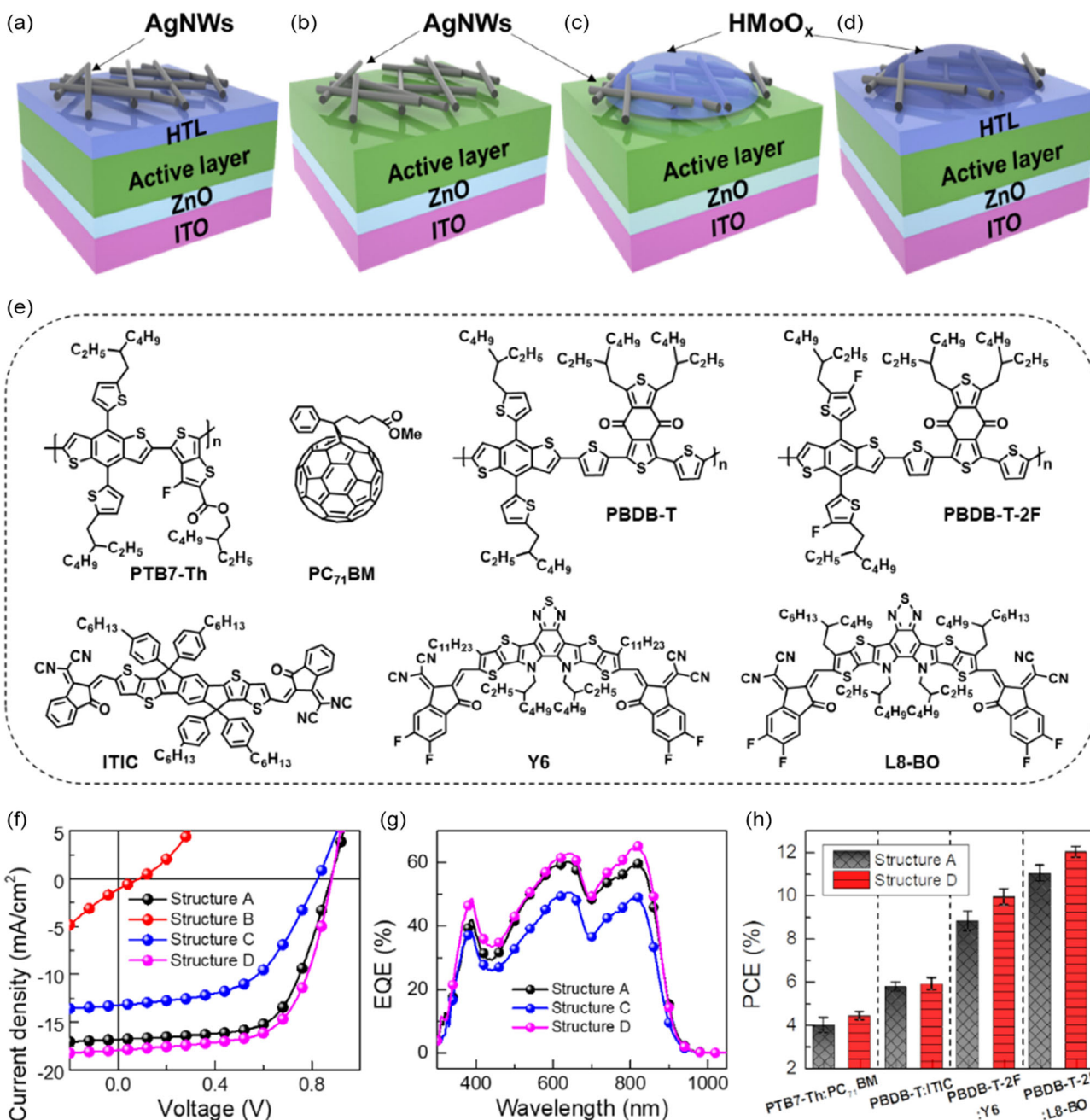


**Figure 3.** a–d) Schematic diagram of the four different structures of the OSCs. e) The molecular structure of active layer materials. f) The  $J-V$  and g) EQE curves of three kinds of devices. h) PCE statistics with different materials.

**Table 1.** The parameter of four kinds of solution-processed PBDB-T-2F:L8-BO OSCs.

Device structure <sup>a)</sup>	$V_{oc}$ [V]	$J_{sc}$ [ $\text{mA cm}^{-2}$ ]	$J_{sc}$ [EQE]	FF [%]	PCE [%]	$R_s$ [ $\Omega \text{ cm}^2$ ]	AVT [%]
(A) ITO/ZnO/Active layer/HTL/AgNWs	0.869 [0.864 ± 0.005]	18.49 [18.40 ± 0.10]	17.94	71.01 [68.30 ± 2.70]	11.41 [11.04 ± 0.37]	5.1	20.51
(B) ITO/ZnO/Active layer/AgNWs	0.080 [0.060 ± 0.021]	0.76 [0.59 ± 0.16]	–	32.89 [29.33 ± 3.56]	0.02 [0.02 ± 0.01]	108.6	20.96
(C) ITO/ZnO/Active layer/AgNWs-HMoO <sub>x</sub>	0.820 [0.814 ± 0.006]	13.31 [13.19 ± 0.13]	13.16	53.96 [49.52 ± 4.45]	5.78 [5.16 ± 0.62]	12.4	20.86
(D) ITO/ZnO/Active layer/HTL/AgNWs-HMoO <sub>x</sub>	0.878 [0.872 ± 0.005]	18.64 [18.54 ± 0.09]	18.27	74.97 [72.11 ± 2.83]	12.27 [12.02 ± 0.25]	4.6	20.36

<sup>a)</sup>The average performance was calculated from eight individual devices, and the device area is 0.09 cm<sup>2</sup>.

To further illustrate the universality of this bulk contact electrode-interface structure in the full-solution-processed OSCs, a series of OSCs with different organic photoactive layers, including PTB7-Th:PC<sub>71</sub>BM, PBDB-T:ITIC, and PBDB-T-2F:Y6 were fabricated. The molecular structures are shown in Figure 3e, and the PCE statistics of the “line-plane” and bulk contact structures (structure A and structure D) are shown in Figure 3h. The detail of *J*-*V* curves and EQE spectra are shown in Figure S4, Supporting Information, and the specific performance parameters of these devices are listed in Table 2. As shown in Figure 3h and Table 2, all the PTB7-Th:PC<sub>71</sub>BM, PBDB-T:ITIC, and PBDB-T-2F:Y6 OSCs showed a significantly improved performance with structure D relative to structure A. In detail, the PCE of PTB7-Th:PC<sub>71</sub>BM, PBDB-T:ITIC, and PBDB-T-2F:Y6 was improved from 4.33%, 6.08%, 9.27% to 4.61%, 6.18%, and 10.30%, respectively. Similarly, devices with structure D presented a much higher FF than those devices with structure A.

In bulk contact electrode-interface structure, different interface materials can be used, such as PEDOT:PSS (AI 4083), which is a classic water-based HTL for the OSCs with great advantages of high conduction and excellent processing property.<sup>[44]</sup> In the bulk contact top electrode structure, the predeposited AgNWs could effectively regulate the surface energy of the underlying layer, making it more hydrophilic. Thus, it is easier to deposit the hydrophilic materials PEDOT:PSS (AI 4083) on it. Figure S5a,b, Supporting Information, shows the contact angle of PEDOT:PSS aqueous solution on the top of the PBDB-T-2F:L8-BO and PBDB-T-2F:L8-BO/AgNWs films. The contact angle of PEDOT:PSS aqueous solution on PBDB-T-2F:L8-BO film is larger than 90°, and the contact angle of PEDOT:PSS solution on PBDB-T-2F:L8-BO/AgNWs film is 56.07°, suggesting the hydrophilicity of PBDB-T-2F:L8-BO/AgNWs surface, which is suitable to the injection of the water-based interface layer. Furthermore, Figure S5c, Supporting Information, shows the *J*-*V* curves of devices with/without PEDOT:PSS (structure A and structure D), and the specific performance parameters are listed in Table 2. Here, the device with “line-plane” contact (structure A) achieves a PCE of 11.65%, with *V*<sub>OC</sub> of 0.879 V, *J*<sub>SC</sub> of

18.51 mA cm<sup>-2</sup>, FF of 71.52%, which is lower than that of bulk contact device (structure D), which has a PCE of 12.16%, with *V*<sub>OC</sub> 0.878 V, *J*<sub>SC</sub> 18.44 mA cm<sup>-2</sup>, FF 75.10%. These results demonstrated the advantage of top injection PEDOT:PSS, and shown the universality of injection materials selection in bulk contact structure. Besides, the top injection can also reduce the solvent erosion between the AgNWs electrode and interface layer. Figure S6, Supporting Information, shows the UV-vis spectra of HMoO<sub>x</sub>:PEDOT:PSS films before/after solvent treatment by spray-coating. The decrease of peak intensity demonstrated that the solvent of AgNWs could cause damage of the HTL during the AgNWs preparation process. The extra interface materials by top injection will avoid the destruction from solvent.

Furthermore, the bulk contact top electrodes can also be applied in the conventional OSCs, which contained a structure of ITO/PEDOT:PSS/active layer/ETL/AgNWs. Two kinds of ETLs, ZnO and PFN-Br were used in this work. As shown by Figure S7, Supporting Information, and Table 2, the devices with bulk contact structure presented higher efficiency (ZnO: 10.79% > 7.76% and PFN-Br: 6.38% > 1.34%). Take the ZnO ETL as an instance, the device with a “line-plane” contact structure showed a *V*<sub>OC</sub> of 0.834 V, a *J*<sub>SC</sub> of 18.67 mA cm<sup>-2</sup>, an FF of 50.02%, and a PCE of 7.76%. In contrast, the *V*<sub>OC</sub>, *J*<sub>SC</sub>, FF, and PCE of bulk contact structure devices increased to 0.841 V, 18.86 mA cm<sup>-2</sup>, 68.03%, and 10.79%. Like the inverted devices, the bulk contact top electrode induced the improvement of full-solution-processed device performance. In summary, the universality of this bulk contact electrode-interface structure has been proved in full-solution-processed OSCs with different active layers, interface materials, and device structures.

To investigate the influence of bulk contact electrode-interface structure on the internal electrical characteristics of OSCs, especially the diode characteristics, device charge transport, the dark *J*-*V* curves, transient photocurrent (TPC), impedance spectrum (EIS), and the light intensity dependence of *V*<sub>OC</sub> and *J*<sub>SC</sub> of the devices were characterized and analyzed. Here, the inverted devices with PBDB-T-2F:L8-BO active layer were investigated.

**Table 2.** The parameter of OSCs with different materials and structure.

Structure <sup>a)</sup>	<i>V</i> <sub>OC</sub> [V]	<i>J</i> <sub>SC</sub> [mA cm <sup>-2</sup> ]	FF [%]	PCE [%]
(A) ITO/ZnO/PTB7-Th:PC <sub>71</sub> BM/HTL/AgNWs	0.789 [0.785 ± 0.003]	9.18 [8.85 ± 0.22]	59.78 [57.63 ± 2.15]	4.33 [3.98 ± 0.35]
(D) ITO/ZnO/PTB7-Th:PC <sub>71</sub> BM/HTL/AgNWs-HMoO <sub>x</sub>	0.787 [0.783 ± 0.003]	9.33 [8.93 ± 0.39]	62.77 [60.11 ± 2.65]	4.61 [4.42 ± 0.19]
(A) ITO/ZnO/PBDB-T:ITIC/HTL/AgNWs	0.837 (0.827 ± 0.008)	13.10 (12.68 ± 0.42)	55.45 (51.94 ± 3.50)	6.08 (5.77 ± 0.31)
(D) ITO/ZnO/PBDB-T:ITIC/HTL/AgNWs-HMoO <sub>x</sub>	0.838 [0.829 ± 0.007]	13.29 [12.72 ± 0.57]	55.51 [53.08 ± 2.43]	6.18 [5.91 ± 0.27]
(A) ITO/ZnO/PBDB-T-2F:Y6/HTL/AgNWs	0.819 [0.815 ± 0.003]	17.53 [17.22 ± 0.31]	64.57 [61.84 ± 2.72]	9.27 [8.82 ± 0.45]
(D) ITO/ZnO/PBDB-T-2F:Y6/HTL/AgNWs-HMoO <sub>x</sub>	0.831 [0.826 ± 0.004]	17.71 [17.50 ± 0.27]	69.98 [67.53 ± 2.44]	10.30 [9.93 ± 0.37]
(A) ITO/ZnO/PBDB-T-2F:L8-BO/HTL/AgNWs	0.879 [0.876 ± 0.004]	18.51 [18.29 ± 0.12]	71.52 [69.83 ± 1.08]	11.65 [11.19 ± 0.25]
(D) ITO/ZnO/PBDB-T-2F:L8-BO/HTL/AgNWs-PEDOT:PSS	0.878 [0.878 ± 0.005]	18.44 [18.13 ± 0.21]	75.10 [73.96 ± 1.26]	12.16 [11.77 ± 0.31]
ITO/PEDOT:PSS/PBDB-T-2F:L8-BO/ZnO/AgNWs	0.831 [0.826 ± 0.004]	18.67 [18.31 ± 0.35]	50.02 [46.81 ± 3.21]	7.76 [7.52 ± 0.24]
ITO/PEDOT:PSS/PBDB-T-2F:L8-BO/ZnO/AgNWs-ZnO	0.841 [0.839 ± 0.002]	18.86 [18.61 ± 0.25]	68.03 [65.87 ± 2.15]	10.79 [10.41 ± 0.38]
ITO/PEDOT:PSS/PBDB-T-2F:L8-BO/PFN-Br/AgNWs	0.699 [0.687 ± 0.012]	10.12 [9.48 ± 0.63]	18.94 [13.65 ± 5.27]	1.34 [0.80 ± 0.54]
ITO/PEDOT:PSS/PBDB-T-2F:L8-BO/PFN-Br/AgNWs-PFN-Br	0.842 [0.839 ± 0.003]	16.48 [16.15 ± 0.33]	45.68 [42.55 ± 3.13]	6.38 [5.93 ± 0.45]

<sup>a)</sup>The average performance was calculated from eight individual devices, and the device area is 0.09 cm<sup>2</sup>.

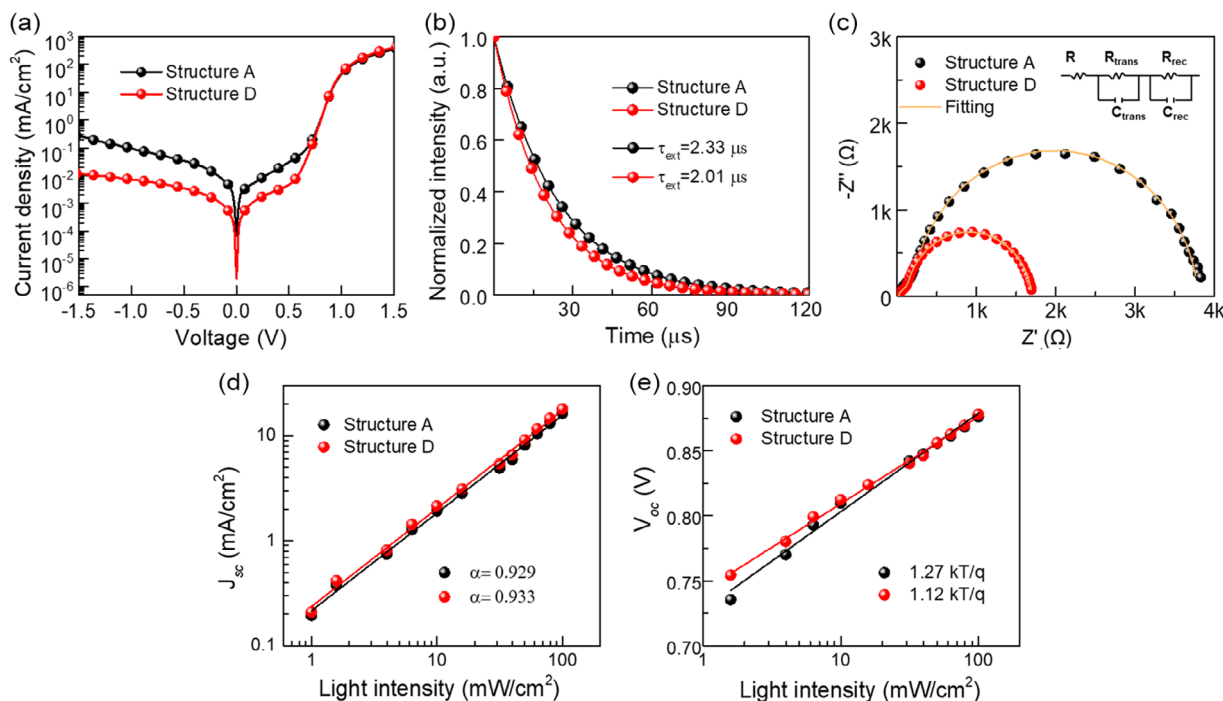
Figure 4a shows the dark  $J-V$  curves of the traditional “line-plane” contact (structure A) and the bulk contact electrode-interface structure devices (structure D). Based on the dark  $J-V$  curves, the rectification ratio of structure A and structure D devices, which is the ratio between forward current (1.5 V) and backward current (−1.5 V),<sup>[45]</sup> was calculated to be 1300 and 34 800, respectively. The significantly improved rectification ratio of structure D relative to structure A indicated the bulk contact electrode-interface structure is more conducive to selectively change charge at the interface in full-solution-processed OSCs. In addition, according to the transient photocurrent (TPC)<sup>[46]</sup> of structure A and structure D device, as shown in Figure 4b, the charge extraction time ( $\tau_{\text{ext}}$ ) of the two structures device is calculated to be 2.33 and 2.01  $\mu\text{s}$ , and the bulk contact structure has a shorter charge extraction time, indicating fast charge extraction in the bulk contact device.

Figure 4c shows the impedance spectrum of structure A and structure D. These curves are presented as an asymmetric semicircle, and the fitted equivalent circuit model<sup>[47]</sup> is shown in Figure 4c. The equivalent circuit model consists of three resistors, which are series resistors  $R$ , transmission resistance  $R_{\text{trans}}$ , composite resistance  $R_{\text{rec}}$ , and two capacitors  $C_{\text{trans}}$  and  $C_{\text{rec}}$ . For device A and device D, the resistors  $R_{\text{rec}}$  are 25 and 17  $\Omega$ , respectively; the transmission resistance  $R_{\text{trans}}$  are 168 and 108  $\Omega$ , and the composite resistance  $R_{\text{rec}}$  are 3600 and 4560  $\Omega$ . The series resistance  $R$  and transmission resistance  $R_{\text{trans}}$  of structure D is lower than that of structure A, and the composite resistance  $R_{\text{rec}}$  of structure D is larger. It is proved that the construction of the bulk contact electrode-interface structure is beneficial to charge transfer and the reduction of charge recombination.

Besides, the light intensity ( $I$ ) dependence of  $J_{\text{SC}}$  was investigated to study the carrier recombination of devices with structures A and D (as shown in Figure 4d). Based on the power law  $J_{\text{SC}} \propto I^\alpha$ , the value of  $\alpha$  represents the degree of bimolecular recombination.<sup>[48]</sup> The  $\alpha$  value of structure D (0.933) is slightly higher than that of structure A (0.929), indicating that the bulk contact structure can slightly suppress the bimolecular recombination. Meanwhile, the light intensity dependence of  $V_{\text{OC}}$  is illustrated in Figure 4e. The device ideal factor  $n$  could be calculated by the equation of  $V_{\text{OC}} = (nk_{\text{B}}T/q)\ln(J_{\text{ph}}/J_0 + 1)$ , where  $k_{\text{B}}$  is the Boltzmann constant,  $T$  is the temperature, and  $J_0$  is the reverse saturation current density.<sup>[49]</sup> The ideal factor  $n$  for OSCs of structure A and structure D is 1.27 and 1.12, respectively, which indicates that the device with structure D has weak bimolecular recombination and suppressed trap-assisted recombination, accounting for the improvement of FF.<sup>[48,50]</sup> This result is consistent with the previous results, proving the advantage of the bulk contact electrode-interface structure in full-solution-processed cells.

### 2.3. Full-Solution-Processed Semitransparent Mini-Module

Based on the bulk contact electrode-interface structure, a 10.8  $\text{cm}^2$  full-solution-processed semitransparent mini-module with PBDB-T-2F:L8-BO materials and area of 10.8  $\text{cm}^2$  was fabricated, and the results are shown in Figure 5. Figure 5a,b shows the schematic diagram and photographs of the inverted full-solution-processed semitransparent mini-module. For this mini-module, the AgNWs top electrode was prepared by spray coating, and the other functional layers were prepared by doctor-blade coating. This mini-module is composed of three



**Figure 4.** Physical characterization of “line-plane” contact and bulk contact device: a) The dark  $J-V$  characteristic, b) normalized TPC curves, c) electrochemical impedance spectroscopy (EIS), d) light intensity-dependent of  $J_{\text{SC}}$ , and e) light intensity-dependent of  $V_{\text{OC}}$ .

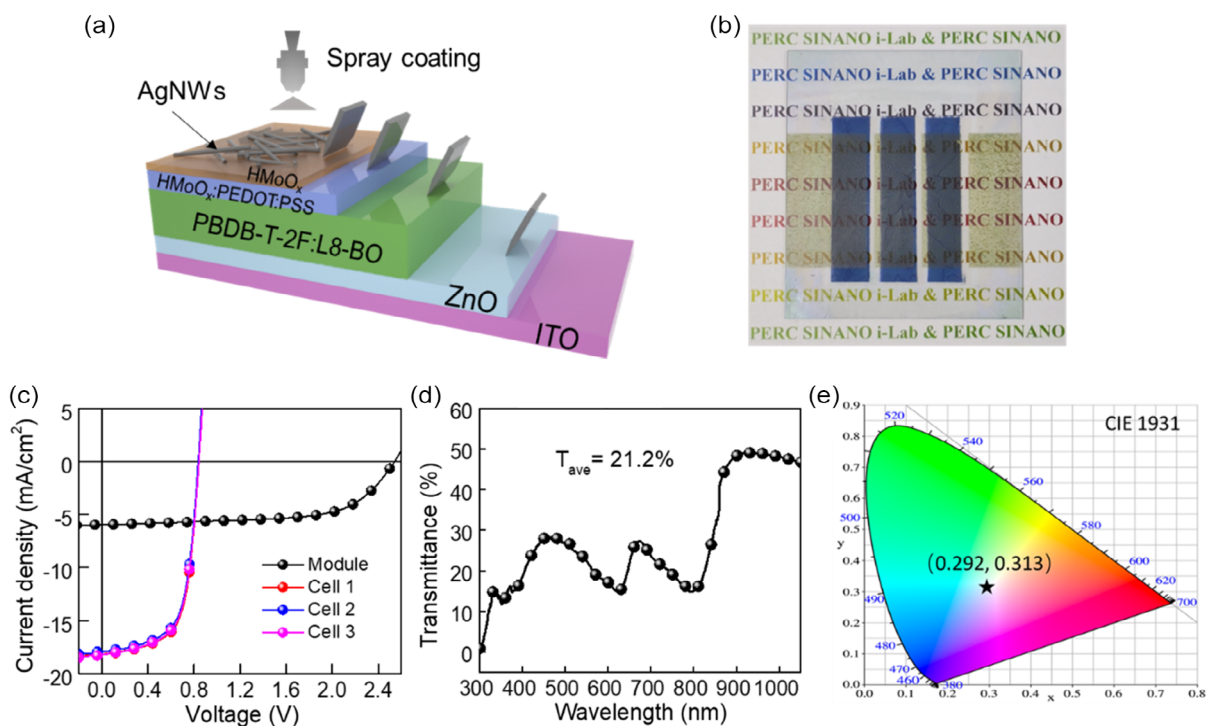


**Figure 5.** a) The structure, b) photograph, c)  $J$ - $V$  characteristics, d) transmission of the semitransparent modules, and e) color coordinates in the CIE 1931 chromaticity diagram of the mini-module.

**Table 3.** The performance of the full-solution processed mini-module.

Device	Area [cm <sup>2</sup> ]	$V_{OC}$ [V]	$J_{SC}$ [mA [cm <sup>2</sup> ] <sup>-2</sup> ]	FF [%]	PCE [%]
Module	10.8	2.541	5.96	63.01	9.54
Cell 1	3.6	0.840	17.84	64.84	9.74
Cell 2		0.836	17.91	64.98	9.73
Cell 3		0.842	18.19	64.38	9.86

subcells in series, each subcell has an area of 3.6 cm<sup>2</sup>. Figure 5c shows the device  $J$ - $V$  curve which was measured with illumination from the ITO side, and the specific parameters are listed in Table 3. As we can see here, the mini-module showed a high PCE of 9.54% ( $V_{OC} = 2.541$  V,  $J_{SC} = 5.96$  mA cm<sup>-2</sup>, FF = 63.01%). In addition, Figure 5d shows the transmittance spectra of the semitransparent mini-module over 300–1100 nm. Based on the transmittance spectra, the average transmittance was calculated to be 21.2%, and the color rendering index CRI is 83.51%.<sup>[51]</sup> Besides, the color coordinate was calculated to be (0.292, 0.313),<sup>[3]</sup> and the CIE diagram was shown in Figure 5e.

### 3. Conclusion

In this work, we propose a bulk contact electrode-interface structure based on the solution-processable AgNWs electrode for the high-efficiency full-solution mini-module. Compared with the traditional “line-plane” contact electrode-interface structure, the bulk contact electrode-interface structure increases the

contact area between the AgNWs electrode and interface buffer layer. This structure improves the charge transfer property between the electrode and the interface, and reduced the charge recombination. Besides, we also demonstrate the universality of this bulk contact electrode-interface structure in different photoactive material systems, interface materials, and device structures. Finally, based on the bulk contact electrode-interface structure, we realize a full-solution-processed semitransparent mini-module preparation with an area of 10.8 cm<sup>2</sup> with an average transmittance of 21.2% and a high PCE of 9.54%. The results provide a new idea for the performance optimization of full-solution-processed OSCs.

### Supporting Information

Supporting Information is available from the Wiley Online Library or from the author.

### Acknowledgements

This work was supported by the National Natural Science Foundation of China (22135001), Youth Innovation Promotion Association (2019317), Young Cross Team Project of CAS (no. JCTD-2021-14), CAS-CSIRO joint project (121E32KYSB20190021) of Chinese Academy of Sciences, Science and Technology Program of Suzhou (ST202219), “Dual Carbon” Science and Technology Innovation of Jiangsu province (Industrial Prospect and Key Technology Research program) (BE2022021). The authors are grateful for the technical support for Nano-X from Suzhou Institute of Nano-Tech and Nano-Bionics, Chinese Academy of Sciences (A2107).



## Conflict of Interest

The authors declare no conflict of interest.

## Data Availability Statement

The data that support the findings of this study are available from the corresponding author upon reasonable request.

## Keywords

bulk contact, interface, organic solar cells, silver nanowires, solution-process

Received: May 2, 2023

Revised: June 29, 2023

Published online: July 25, 2023

- [1] Y. Han, X. Chen, J. Wei, G. Ji, C. Wang, W. Zhao, J. Lai, W. Zha, Z. Li, L. Yan, H. Gu, Q. Luo, Q. Chen, L. Chen, J. Hou, W. Su, C.-Q. Ma, *Adv. Sci.* **2019**, *6*, 1901490.
- [2] W. Song, K. Yu, E. Zhou, L. Xie, L. Hong, J. Ge, J. Zhang, X. Zhang, R. Peng, Z. Ge, *Adv. Funct. Mater.* **2021**, *31*, 2102694.
- [3] D. Xie, Y. Zhang, X. Yuan, Y. Li, F. Huang, Y. Cao, C. Duan, *Adv. Funct. Mater.* **2022**, *33*, 2212601.
- [4] J. Wei, C. Zhang, G. Ji, Y. Han, I. Ismail, H. Li, Q. Luo, J. Yang, C.-Q. Ma, *Solar Energy* **2019**, *193*, 102.
- [5] A. Armin, W. Li, O. J. Sandberg, Z. Xiao, L. Ding, J. Nelson, D. Neher, K. Vandewal, S. Shoaee, T. Wang, H. Ade, T. Heumüller, C. Brabec, P. Meredith, *Adv. Energy Mater.* **2021**, *11*, 2003570.
- [6] Y. Wang, Z. Zheng, J. Wang, X. Liu, J. Ren, C. An, S. Zhang, J. Hou, *Adv. Mater.* **2022**, *35*, 2208305.
- [7] W. Gao, F. Qi, Z. Peng, F. R. Lin, K. Jiang, C. Zhong, W. Kaminsky, Z. Guan, C.-S. Lee, T. J. Marks, H. Ade, A. K.-Y. Jen, *Adv. Mater.* **2022**, *34*, 2202089.
- [8] Y. Wei, Z. Chen, G. Lu, N. Yu, C. Li, J. Gao, X. Gu, X. Hao, G. Lu, Z. Tang, J. Zhang, Z. Wei, X. Zhang, H. Huang, *Adv. Mater.* **2022**, *34*, 2204718.
- [9] W. Liu, S. Sun, S. Xu, H. Zhang, Y. Zheng, Z. Wei, X. Zhu, *Adv. Mater.* **2022**, *34*, 2200337.
- [10] Y. Zhao, Z. Li, C. Deger, M. Wang, M. Peric, Y. Yin, D. Meng, W. Yang, X. Wang, Q. Xing, B. Chang, E. G. Scott, Y. Zhou, E. Zhang, R. Zheng, J. Bian, Y. Shi, I. Yavuz, K.-H. Wei, K. N. Houk, Y. Yang, *Nat. Sustain.* **2023**, *6*, 539.
- [11] Y. Li, X. Huang, H. K. M. Sheriff, S. R. Forrest, *Nat. Rev. Mater.* **2023**, *8*, 186.
- [12] Q. Liu, L. G. Gerling, F. Bernal-Texca, J. Toudert, T. Li, X. Zhan, J. Martorell, *Adv. Energy Mater.* **2020**, *10*, 1904196.
- [13] X. Sun, W. Zha, T. Lin, J. Wei, I. Ismail, Z. Wang, J. Lin, Q. Luo, C. Ding, L. Zhang, Z. Su, B. Chu, D. Zhang, C.-Q. Ma, *J. Mater. Sci.* **2020**, *55*, 14893.
- [14] Y. Jiang, T. Liu, Y. Zhou, *Adv. Funct. Mater.* **2020**, *30*, 2006213.
- [15] H. Park, J.-H. Lee, S. Lee, S. Y. Jeong, J. W. Choi, C.-L. Lee, J.-H. Kim, K. Lee, *ACS Appl. Mater. Interfaces* **2020**, *12*, 2276.
- [16] J. Wan, X. Fan, H. Huang, J. Wang, Z. Zhang, J. Fang, F. Yan, *J. Mater. Chem. A* **2020**, *8*, 21007.
- [17] P. M. Rajanna, H. Meddeb, O. Sergeev, A. P. Tsapenko, S. Bereznev, M. Vehse, O. Volobujeva, M. Danilson, P. D. Lund, A. G. Nasibulin, *Nano Energy* **2020**, *67*, 104183.
- [18] Y. Song, S. Chang, S. Gradedecak, J. Kong, *Adv. Energy Mater.* **2016**, *6*, 1600847.
- [19] T. Sanniccolo, M. Lagrange, A. Cabos, C. Celle, J.-P. Simonato, D. Bellet, *Small* **2016**, *12*, 6052.
- [20] D. Tan, C. Jiang, Q. Li, S. Bi, J. Song, *J. Mater. Sci. Mater. Electron.* **2020**, *31*, 15669.
- [21] X. He, Y. Wang, L. Zhang, R. Zhang, J. Kim, K. S. Wong, Y. Chen, W. C. H. Choy, *Adv. Funct. Mater.* **2021**, *31*, 2010764.
- [22] H. Tang, H. Feng, H. Wang, X. Wan, J. Liang, Y. Chen, *ACS Appl. Mater. Interfaces* **2019**, *11*, 25330.
- [23] H. Sohn, C. Park, J.-M. Oh, S. W. Kang, M.-J. Kim, *Materials* **2019**, *12*, 2526.
- [24] K. Han, M. Xie, L. Zhang, L. Yan, J. Wei, G. Ji, Q. Luo, J. Lin, Y. Hao, C.-Q. Ma, *Sol. Energy Mater. Sol. Cells* **2018**, *185*, 399.
- [25] M. Xie, H. Lu, L. Zhang, J. Wang, Q. Luo, J. Lin, L. Ba, H. Liu, W. Shen, L. Shi, C.-Q. Ma, *Sol. RRL* **2018**, *2*, 1700184.
- [26] Z. Wang, Y. Han, L. Yan, C. Gong, J. Kang, H. Zhang, X. Sun, L. Zhang, J. Lin, Q. Luo, C. Q. Ma, *Adv. Funct. Mater.* **2020**, *31*, 2007276.
- [27] Y. Xiong, R. E. Booth, T. Kim, L. Ye, Y. Liu, Q. Dong, M. Zhang, F. So, Y. Zhu, A. Amassian, B. T. O'Connor, H. Ade, *Sol. RRL* **2020**, *4*, 2000328.
- [28] L. Duan, B. Hoex, A. Uddin, *Sol. RRL* **2021**, *5*, 2100041.
- [29] S. Han, Y. Deng, W. Han, G. Ren, Z. Song, C. Liu, W. Guo, *Solar Energy* **2021**, *225*, 97.
- [30] Y. Sun, B. Mayers, T. Herricks, Y. Xia, *Nano Lett.* **2003**, *3*, 955.
- [31] Y. Ge, X. Duan, M. Zhang, L. Mei, J. Hu, W. Hu, X. Duan, *J. Am. Chem. Soc.* **2018**, *140*, 193.
- [32] D. P. Langley, M. Lagrange, G. Giusti, C. Jimenez, Y. Brechet, N. D. Nguyen, D. Bellet, *Nanoscale* **2014**, *6*, 13535.
- [33] J. H. Park, G.-T. Hwang, S. Kim, J. Seo, H.-J. Park, K. Yu, T.-S. Kim, K. J. Lee, *Adv. Mater.* **2017**, *29*, 1603473.
- [34] G. Zeng, W. Chen, X. Chen, Y. Hu, Y. Chen, B. Zhang, H. Chen, W. Sun, Y. Shen, Y. Li, F. Yan, Y. Li, *J. Am. Chem. Soc.* **2022**, *144*, 8658.
- [35] W. Xiong, H. Liu, Y. Chen, M. Zheng, Y. Zhao, X. Kong, Y. Wang, X. Zhang, X. Kong, P. Wang, L. Jiang, *Adv. Mater.* **2016**, *28*, 7167.
- [36] J. Huang, Z. Lu, J. He, H. Hu, Q. Liang, K. Liu, Z. Ren, Y. Zhang, H. Yu, Z. Zheng, G. Li, *Energy Environ. Sci.* **2023**, *16*, 1251.
- [37] C.-C. Chen, L. Dou, R. Zhu, C.-H. Chung, T.-B. Song, Y. B. Zheng, S. Hawks, G. Li, P. S. Weiss, Y. Yang, *ACS Nano* **2012**, *6*, 7185.
- [38] L. K. Jagadamma, H. Hu, T. Kim, G. O. N. Ndjawa, A. E. Mansour, A. El Labban, J. C. D. Faria, R. Munir, D. H. Anjum, M. A. McLachlan, A. Amassian, *Nano Energy* **2016**, *28*, 277.
- [39] L. Sun, W. Zeng, C. Xie, L. Hu, X. Dong, F. Qin, W. Wang, T. Liu, X. Jiang, Y. Jiang, Y. Zhou, *Adv. Mater.* **2020**, *32*, 1907840.
- [40] L. Lucera, F. Machui, H. D. Schmidt, T. Ahmad, P. Kubis, S. Strohm, J. Hepp, A. Vetter, H. J. Egelhaaf, C. J. Brabec, *Org. Electron.* **2017**, *45*, 209.
- [41] W. Jo, H. S. Kang, J. Choi, H. Lee, H.-T. Kim, *ACS Appl. Mater. Interfaces* **2017**, *9*, 15114.
- [42] G. Ji, Y. Wang, Q. Luo, K. Han, M. Xie, L. Zhang, N. Wu, J. Lin, S. Xiao, Y.-Q. Li, L.-Q. Luo, C.-Q. Ma, *ACS Appl. Mater. Interfaces* **2018**, *10*, 943.
- [43] S. Wageh, M. Raïssi, T. Berthelot, A. A. Al-Ghamdi, A. M. Abusorrah, W. Boukhili, O. A. Al-Hartomy, *Adv. Eng. Mater.* **2021**, *23*, 2001305.
- [44] Y. Jiang, X. Dong, L. Sun, T. Liu, F. Qin, X. Lu, X. Zhou, W. Meng, N. Li, C. Xie, P. Jiang, C. J. Brabec, L. Hu, Y. Zhou, *Nat. Energy* **2022**, *7*, 352.
- [45] S. K. Gautam, A. Das, R. G. Singh, V. V. S. Kumar, F. Singh, *J. Appl. Phys.* **2016**, *120*, 214502.
- [46] X. Xu, L. Yu, H. Meng, L. Dai, H. Yan, R. Li, Q. Peng, *Adv. Funct. Mater.* **2021**, *32*, 2108797.
- [47] L. Lu, Q. Liao, Y. Zu, Y. Xu, B. Xu, J. Hou, *Adv. Energy Mater.* **2019**, *9*, 1803826.

- [48] Q. Huang, J. Jing, K. Zhang, Y. Chen, A. Song, Z. Liu, F. Huang, *J. Mater. Chem. A* **2022**, *10*, 23973.
- [49] W. Pan, Y. Han, Z. Wang, C. Gong, J. Guo, J. Lin, Q. Luo, S. Yang, C.-Q. Ma, *J. Mater. Chem. A* **2021**, *9*, 16889.
- [50] L. Wu, H. Zang, Y.-C. Hsiao, X. Zhang, B. Hu, *Appl. Phys. Lett.* **2014**, *104*, 153903.
- [51] C. Yang, D. Liu, M. Bates, M. C. Barr, R. R. Lunt, *Joule* **2019**, *3*, 1803.